Environmental Science & Technology

pubs.acs.org/est

Article

Enhancing Performance of Capacitive Deionization with Polyelectrolyte-Infiltrated Electrodes: Theory and Experimental Validation

Li Wang,* Yuanzhe Liang, and Li Zhang*

Cite This: *Environ. Sci. Technol.* 2020, 54, 5874−5883

Read Online

ACCESS | Metrics & More | Article Recommendations | Supporting Information

ABSTRACT: The energy efficiency of capacitive deionization (CDI) with porous carbon electrodes is limited by the high ionic resistance of the macropores in the electrodes. In this study, we demonstrate a facile approach to improve the energy efficiency by filling the macropores with ion-conductive polyelectrolytes, which is termed polyelectrolyte-infiltrated CDI (pie-CDI or πCDI). In πCDI, the filled polyelectrolyte effectively turns the macropores into a charged ion-selective layer and thus increases the conductivity of macropores. We show experimentally that πCDI can save up to half of the energy consumption compared to membrane CDI, achieving identical desalination during the charging step. The energy consumption can be even lower if the process is operated at a smaller average salt adsorption rate. Further energy breakdown analysis based on a theoretical model confirms that the improved energy efficiency is largely attributed to the increased conductivity in the macropores.

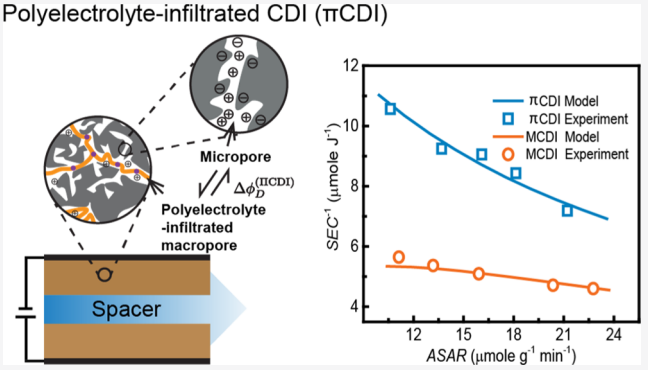

INTRODUCTION

Capacitive deionization (CDI) has experienced a dramatic growth over the past decades because of its promising prospects in desalination of brackish water. In CDI, ions are adsorbed in the electrical double layer (EDL) formed at the interface between the electrode matrix and the aqueous solution when a small voltage bias is applied across two porous electrodes, while simultaneously electric charges are stored at the interface.[1] The energy spent in the adsorbing/charging step could be partially recovered in the desorbing/discharging step.[2−4] As a separation process with a simple setup, tunable salt rejection, and flexible scalability, CDI is considered to be a competitive alternative to some state-of-the-art desalination technologies.

The electrode materials are critical to the performance of CDI.[1] Efforts for high-performance CDI electrodes have mainly focused on increasing the electrode adsorption capacity,[5−8] enabling long-term stability,[9−11] introducing selectivity by modifying the surface chemistry,[12−17] and enhancing charge efficiency by Faradaic reactions.[18,19] Regardless of the different approaches, the ultimate goal of developing novel electrode materials for CDI is to achieve a desalination process that consumes less energy and achieves an appealing desalting rate. Based on an energy breakdown analysis, it has been demonstrated that the energy loss not only occurs in the electrical circuit including the contact resistance but also occurs in other components including the electrode macropores.[20−23] The energy loss in the macropores could be especially significant if the concentration inside is low when treating low-salinity brackish water.

One way to reduce the macropore resistance is to incorporate ion-exchange membranes (IEMs) in front of the porous electrodes, *that is*, membrane CDI (MCDI), which blocks the repulsion of co-ions (*i.e.*, ions having the same charge sign as the electrode) and therefore increases the charge efficiency and the macropore concentration.[24−26] Nevertheless, the IEMs can only amplify the macropore concentration several times relative to the spacer concentration, and thus, the improvement of the macropore conductivity is very limited. In addition, the presence of IEMs introduces extra electrical resistance.

Here, we demonstrate a new method by infiltrating an ion-conductive polyelectrolyte to the macropores of the carbon electrodes to improve the kinetic and energetic efficiencies. We use Nafion[27,28] to infiltrate the cathode and quaternized poly(2,6-dimethyl-1,4-phenylene oxide) (QPPO) to infiltrate the anode.[27,28] Activated carbon cloth (ACC) is used as the

Received: December 17, 2019
Revised: March 26, 2020
Accepted: March 27, 2020
Published: March 27, 2020

https://dx.doi.org/10.1021/acs.est.9b07692
Environ. Sci. Technol. 2020, 54, 5874−5883

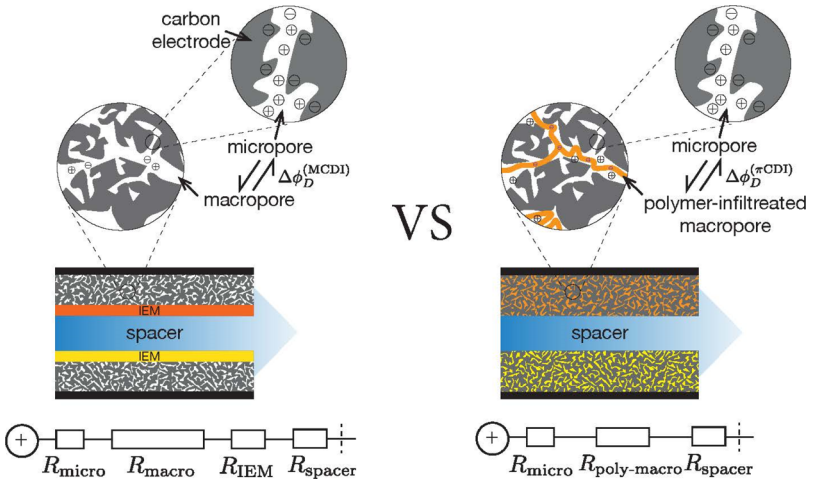

Figure 1. Schematics of MCDI (left) and CDI with polyelectrolyte-infiltrated electrodes, πCDI (right).

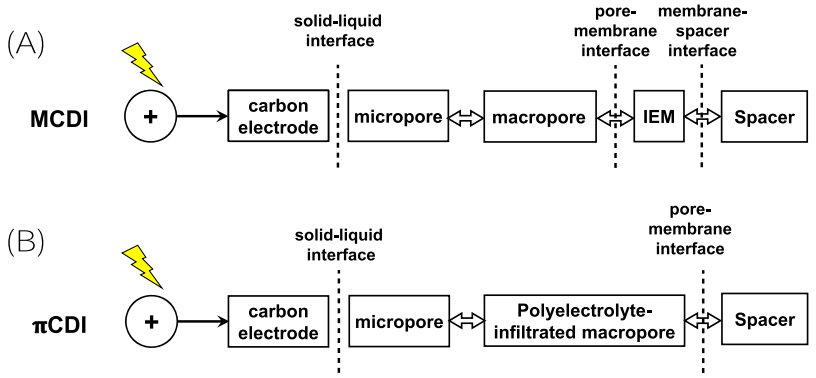

Figure 2. Graphic illustration of models for the half cell of MCDI (A) and πCDI (B). The double thick arrow indicates that the Donnan equilibrium is assumed at the interface.

platform to provide large voids for the infiltration, while maintaining the electrical conductive skeleton.[29] The shape flexibility and economic accessibility make ACC a good candidate for CDI electrodes. There are only few recent studies on ion-conductive polyelectrolyte for the CDI electrode. Bhat *et al.* carved the activated carbon electrode in patterned grooves that then were coated with the conductive polyelectrolyte in order to improve the electrode tortuosity and conductivity.[30] In another study, Fritz *et al.* ground the charged polymer with activated carbon powder to fabricate the inverted CDI electrodes that adsorb the salt without charging while releasing the salt with charging.[31] Although we take a similar advantage of the ion-conductive polyelectrolyte in the present study, the rationale behind is different, given that we intend to increase the conductivity of the macropores. In the as-prepared polyelectrolyte-infiltrated electrode, the macropores are filled with the charged polyelectrolyte and behave like an ion-selective layer bridging between the spacer and the electrode micropores (Figure 1). Unlike the study presented by Bhat *et al.*, the carbon electrodes were carved with a 100 μm mill before coating with the polyelectrolyte, of which the reduction in tortuosity decreased the impedance of the patterned electrodes. The energy loss in the macropore is reduced because ions migrate more easily from the spacer through the ion-selective layer to the micropores. Moreover, a theoretical model incorporating ion transport is developed for this type of CDI to better understand the underlying process and facilitate the energy breakdown analysis.

In this study, we first present a transport model for CDI with polyelectrolyte-infiltrated electrodes (pie-CDI or πCDI) and compare it with the model for MCDI. Following this modeling approach, we show that πCDI can be seen as a limiting case of MCDI with zero macropore volume. Then, we describe the experimental setups for both MCDI and πCDI. The modeled results and the experimental data are in good agreement via fitting the model with feasible parameters reported in the literature. Furthermore, we analyze the trade-off curve between energy efficiency and desalination rate and the breakdown of energy consumption based on transport models for both setups. Results show that the πCDI systematically outperforms MCDI in both energy and kinetic aspects.

DESCRIPTION OF THE MODEL

To model the charging/discharge process in CDI, we treat the electrode as a dual-porosity material consisting of micropores and macropores. Dynamic ion transport in the macropore and the spacer is described by the Nernst−Planck equation, and local equilibrium is assumed between the macropore and micropore. Then, the charging model in the micropore is specified. In this work, we employ the amphoteric Donnan (amph-D) model that considers the effects of charged groups in the micropores.[32,33] The mathematical treatment for MCDI follows previous studies,[21,34] but the model for the polyelectrolyte-filled macropore is first introduced in this study. For MCDI, the ion transport in the IEM is considered

https://dx.doi.org/10.1021/acs.est.9b07692
Environ. Sci. Technol. 2020, 54, 5874−5883

and the macropore is assumed to be electroneutral, while for πCDI, the macropore is modeled as a charged medium because of the presence of the polyelectrolyte, which behaves similarly to an IEM. In the following derivation, we introduce MCDI before πCDI wherever they are treated differently (*e.g.,* macropores) because the MCDI model is similar to the literature studies. We consider a monovalent salt unless specified otherwise.

Dynamic Transport Model. We consider the ion transport in the spacer channel and the porous electrodes including both micropores and macropores. We assume that the aqueous solution in the porous electrodes and the spacer channel is completely mixed, and thus, neither concentration nor electrical potential gradients exist in either the electrode or the spacer. Besides, the system is assumed to be symmetric, so the difference in diffusion rates between the cation and the anion has been ignored and the charge densities of the polyelectrolyte in the paired πCDI electrodes are same but with different signs (see the Supporting Information for detail). In this way, we can model half of the system, *that* is, one electrode. A general description and comparison of the models for MCDI and πCDI are shown in Figure 2. In the following, we specify the details of the model.

When charging or discharging the electrodes, conservation of electronic charge in the conducting matrix of one electrode gives

$$\frac{\partial}{\partial t}(p_{mi}\sigma_{elec}) = \frac{I}{L_{elec}F} \tag{1}$$

where σ_{elec} is the electric charge density averaged over the micropore volume, p_{mi} is the microporosity of the electrode, I is the electric current density, and L_{elec} is the thickness of one electrode. The ionic charge accumulates in the micropore to balance the electric charge in the electrode matrix. Besides, there is chemical charge formed by functional groups at the electrode−solution interface. Conservation of the total charge in one electrode requires that[12,35,36]

$$\sigma_{elec} + \sigma_{ionic} + \sigma_{chem} = 0 \tag{2}$$

where σ_{ionic} and σ_{chem} are the ionic and chemical charge density averaged over the micropore volume, respectively.

During the charge and discharge steps, the ionic concentrations in the micro- and macropores change as a result of the transport of salt ions. Conservation of the total ion concentration in the porous region of one electrode gives

$$\frac{\partial}{\partial t}\sum_k (p_{mA}c_{mA}^k + p_{mi}c_{mi}^k) = \frac{J_{ions}}{L_{elec}} \tag{3}$$

where J_{ions} is the total ionic flux, c_{mA}^k and c_{mi}^k are the kth ion concentrations in the macropore and micropore, respectively (for single salt, k = 1 for the cation, k = 2 for the anion).

The ion flux to the electrode results in desalination of the feed solution in the spacer channel. The change of salt concentration in the spacer can be written as

$$p_{sp}\frac{\partial c_{sp}}{\partial t} = -\frac{J_{ions}}{L_{sp}} + \frac{c_{sp,0} - c_{sp}}{\tau} \tag{4}$$

where p_{sp} is the spacer porosity, c_{sp} is the salt concentration in the spacer, $c_{sp,0}$ is the feed influent concentration, L_{sp} is the spacer thickness, and τ is the hydraulic retention time in the spacer channel. Because the spacer volume is considered to be well mixed, c_{sp} is also the effluent concentration to be measured experimentally. According to the Nernst−Planck equation, the current density, I, depends on the electric potential difference across the spacer channel and the spacer salt concentration, which can be expressed as

$$I = -4Dc_{sp}\frac{\Delta\phi_{sp,half}}{L_{sp}}F \tag{5}$$

where D is an average bulk diffusion coefficient of the salt ions and $\Delta\phi_{sp,half}$ is the potential drop across half of the spacer. In MCDI, this current density also equals that across the IEM, which can be expressed as

$$I = -D_{mem}\overline{c}_{mem}\frac{\Delta\phi_{mem}}{L_{mem}}F \tag{6}$$

where D_{mem} is the averaged diffusion coefficient of the salt ions in the membrane, $\overline{c}_{mem}$ is the average total ion concentration in the membrane, and L_{mem} is the membrane thickness. For simplicity, $\overline{c}_{mem}$ is approximated as the average of the ion concentrations at the two interfaces of the IEM (*i.e.,* membrane/spacer and membrane/electrode). Because the charge density of the IEM is large, it allows the preferential transport of counterions through. The ion flux in the IEM, J_{ions}, relates to the concentration and potential differences across the IEM

$$J_{ions} = -\frac{D_{mem}}{L_{mem}}(\Delta c_{mem} - \omega X\Delta\phi_{mem}) \tag{7}$$

where Δc_{mem} is the difference between the ion concentrations at the two membrane interfaces (*i.e.,* $c_{mem/elec}$ and $c_{mem/sp}$), ω is the sign of the membrane charge (+1 for anion-exchange membranes and −1 for cation-exchange membranes), and X is the membrane charge density. Note that eqs 6 and 7 are not necessary for πCDI because of the absence of IEMs.

Next, we assume that the Donnan equilibrium is satisfied between the IEM and the macropore, the IEM and the spacer channel in MCDI, and between the spacer channel and the polyelectrolyte-filled macropore, the macropore and the micropore in πCDI (thick double arrows in Figure 2).[37,38] In addition, both the IEMs and the polyelectrolyte-filled macropores are treated as charged porous media, meaning that the ion-conductive macropores filled with the polyelectrolyte in πCDI behave similarly as IEMs.

At the membrane−electrode and the membrane−spacer interfaces in MCDI, according to the Donnan equilibrium, the total ion concentration within the membrane at two interfaces are

$$c_{mem/elec} = 2c_{mA}\cosh(\Delta\phi_{m/elec}) \tag{8}$$

$$c_{mem/sp} = 2c_{sp}\cosh(\Delta\phi_{m/sp}) \tag{9}$$

and the corresponding Donnan potential drops, $\Delta\phi_{m/sp}$ and $\Delta\phi_{m/elec}$, are given by

$$\Delta\phi_{m/elec} = \sinh^{-1}\frac{\omega X}{c_{mA}} \tag{10}$$

$$\Delta\phi_{m/sp} = \sinh^{-1}\frac{\omega X}{c_{sp}} \tag{11}$$

Equations 8−11 can be applied to the polyelectrolyte-infiltrated macropores similarly, leading to

https://dx.doi.org/10.1021/acs.est.9b07692
Environ. Sci. Technol. 2020, 54, 5874−5883

$$c_{\mathrm{mA,pie/mi}} = 2c_{\nu}\cosh(\Delta\phi_{\mathrm{mA,pie/mi}}) \tag{12}$$

$$c_{\mathrm{mA,pie/sp}} = 2c_{\mathrm{sp}}\cosh(\Delta\phi_{\mathrm{mA,pie/sp}}) \tag{13}$$

$$\Delta\phi_{\mathrm{mA,pie/mi}} = \sinh^{-1}\frac{\omega X_{\mathrm{poly}}}{c_{\nu}} \tag{14}$$

$$\Delta\phi_{\mathrm{mA,pie/sp}} = \sinh^{-1}\frac{\omega X_{\mathrm{poly}}}{c_{\mathrm{sp}}} \tag{15}$$

where c_{ν} is the concentration in the small slab that is negligible in volume but connects the micropore and the macropore of πCDI. It is introduced to help calculate the Donnan equilibrium between the macropore and the micropore, but not directly used in the transport equations. Also, X_{poly} is the charge density of the polyelectrolyte.

Following eq 7, the ion flux in the polyelectrolyte-infiltrated macropores is

$$J_{\mathrm{ions}} = -p_{\mathrm{mA}}\frac{D_{\mathrm{mA,pie}}}{L_{\mathrm{elec}}}(\Delta c_{\mathrm{mA,pie}} - \omega X_{\mathrm{poly}}\Delta\phi_{\mathrm{mA,pie}}) \tag{16}$$

where $D_{\mathrm{mA,pie}}$ is the diffusion coefficient in the polyelectrolyte-filling macropores, $\Delta c_{\mathrm{mA,pie}}$ is the difference between the ion concentrations at the two ends of the polyelectrolyte-filling macropores, and $\Delta\phi_{\mathrm{mA,pie}}$ is the potential drop across such macropores.

Micropore Charging Model. We employ the amphoteric Donnan (amph-D) model that considers the effects of charged groups in the micropores of the electrodes.[32] These surface-immobilized charged functional groups (σ_{chem}) together with the mobile ionic charges (σ_{ionic}) balance the electronic charges (σ_{elec}) in the carbon electrode.[12,32,33,35] The amph-D model assumes two types of regions in the micropores: the acidic region named A-region and the basic region named B-region. The A-region may contain groups such as carboxyl, lactone, or phenol and is thus negatively charged, while the B-region has protonated groups that are positively charged.[39,40]

The concentration of ions in the electrode micropores is related to the macropore ion concentration via the Donnan potential across the interface between the micro- and macropores

$$c_{\mathrm{mi},j}{}^{\pm} = c_{\mathrm{mA}}\exp(-z^{\pm}\Delta\phi_{\mathrm{D},j}) \tag{17}$$

where $c_{\mathrm{mi},j}{}^{\pm}$ is the ion concentration in the j-region of the micropores, c_{mA} is the macropore salt concentration, $z^{\pm}$ is the ion charge valence (*e.g.*,, +1 for the monovalent cation and −1 for the monovalent anion), and $\Delta\phi_{\mathrm{D},j}$ is the dimensionless Donnan potential difference between the j-region of the micropores and the macropores. The j-region could be either acidic or basic, *that* is, A- or B-region. For πCDI, c_{mA} should be replaced with c_{ν}.

The volumetric ionic micropore charge density ($\sigma_{\mathrm{ion},j}$) is determined by the cation and anion concentrations in the micropores

$$\sigma_{\mathrm{ionic},j} = c_{\mathrm{mi},j}{}^{+} - c_{\mathrm{mi},j}{}^{-} = -2c_{\mathrm{mA}}\sinh(\Delta\phi_{\mathrm{D},j}) \tag{18}$$

In addition, $\sigma_{\mathrm{elec},j}$ is related to the Stern layer potential difference ($\Delta\phi_{\mathrm{S}}$) and Stern layer capacitance (C_{S})

$$\sigma_{\mathrm{elec},j}F = -C_{\mathrm{S}}\Delta\phi_{\mathrm{S}}V_{\mathrm{T}} \tag{19}$$

where F is the Faraday constant (96,485 C·mol^{-1}) and V_{T} is the thermal voltage that converts the unit to volt (@ room temperature, V_{T} = 25.6 mV).

The average electronic charge density is given by

$$\sigma_{\mathrm{elec}} = \sum \alpha_j\sigma_{\mathrm{elec},j} \tag{20}$$

where σ_{elec} is the average electronic charge density in the micropores of the electrodes and α_j is the fraction of the j-region relative to the total micropore volume. In this study, both α_{A} and α_{B} are assigned as 0.5, and the chemical charges are of the same magnitude but different in sign, *that is*, negative and positive for A- and B-regions, respectively, as they have been treated in the previous studies.[32,35] In other words, the paired electrodes are symmetric.

There is a constraint of the A and B regions, that is, the potential drops over the EDL, $\Delta\phi_{\mathrm{EDL}}$, for each are equal

$$\Delta\phi_{\mathrm{EDL,A}} = \Delta\phi_{\mathrm{EDL,B}} \tag{21}$$

Potential Drops in the System. The potential drop in the porous carbon electrode ($\Delta\phi_{\mathrm{elec}}$) is determined by the salt concentration in the macropores and the current density

$$\Delta\phi_{\mathrm{elec}}V_{\mathrm{T}} = IR_{\mathrm{elec}}/\bar{c}_{\mathrm{mA}} \tag{22}$$

where R_{elec} is the specific electrode resistance and $\bar{c}_{\mathrm{mA}}$ is the average concentration in the electrode macropore, both of which are treated differently for the two kinds of cells. In MCDI, R_{elec} is a fitting parameter that is tuned to match the experimental and modeled results for cell voltage, and we do not consider the concentration gradient along the macropore. With respect to πCDI, $\bar{c}_{\mathrm{mA}}$ is the average concentration of $c_{\mathrm{mA,pie/mi}}$ and $c_{\mathrm{mA,pie/sp}}$, and its R_{elec} is calculated following the equation

$$R_{\mathrm{elec}} = \frac{V_{\mathrm{T}}L_{\mathrm{elec}}}{D_{\mathrm{mA,pie}}Fp_{\mathrm{mA}}} \tag{23}$$

Finally, the CDI cell voltage is simply the twice of the sum of all potential drops from the carbon phase to the spacer channel (assuming symmetric potential distribution between two half cells)

$$V_{\mathrm{cell}} = 2(\Delta\phi_{\mathrm{EDL}} + \Delta\phi_{\mathrm{elec}} + \Delta\phi_{\mathrm{m/sp}} + \Delta\phi_{\mathrm{mem}} - \Delta\phi_{\mathrm{m/elec}} + \Delta\phi_{\mathrm{sp,half}})V_{\mathrm{T}} + IR_{\mathrm{ext}} \tag{24}$$

where R_{ext} (Ω·cm^2) represents all resistances in the external circuit, the current collectors, and the contact resistances between the current collectors and the electrodes. For πCDI, the membrane potential drop is eliminated. The potential drops at the membrane edges, *that is*, $\Delta\phi_{\mathrm{m/sp}}$ and $\Delta\phi_{\mathrm{m/elec}}$ shall be replaced by $\Delta\phi_{\mathrm{mA,pie/sp}}$ and $\Delta\phi_{\mathrm{mA,pie/mi}}$, respectively.

METHODS AND EXPERIMENTS

Electrode Preparation. Electrodes of πCDI were prepared by infiltrating the conductive polyelectrolyte into the ACC (FM 50K, Zorflex, Pittsburg, PA). Two kinds of polyelectrolytes were used, negatively charged Nafion and positively charged QPPO. Nafion and QPPO were used to modify the cathode and anode, respectively. The infiltration of Nafion was conducted by soaking ACC in a 15% wt LIQUION solution (Ion Power Inc., Delaware, USA) for 1 h followed by 1 h drying at 60 °C and 1 h annealing at 140 °C in a vacuum oven. The anion-selective QPPO polyelectrolyte was obtained by

https://dx.doi.org/10.1021/acs.est.9b07692
Environ. Sci. Technol. 2020, 54, 5874−5883

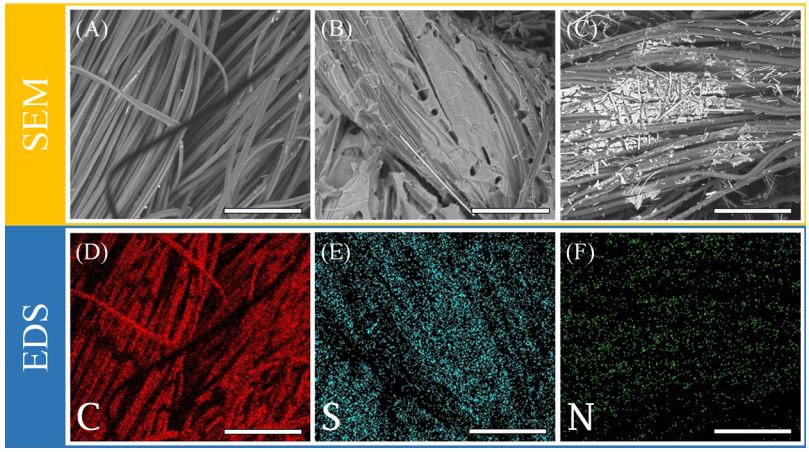

Figure 3. Material characterization. First row: SEM images of pristine (A), Nafion-infiltrated (B) and QPPO-infiltrated (C) ACC electrodes. Second row: EDS elemental mapping of the carbon on pristine (D), sulfur on Nafion-infiltrated (E), and nitrogen on QPPO-infiltrated (F) ACC electrodes. SEM and EDS elemental mapping for the polyelectrolyte-infiltrated electrodes were characterized after the desalination experiments. The white bars in the panels represent 100 μm.

bromination of poly(2,6-dimethyl-1,4-phenylene oxide) (Sigma-Aldrich), following a protocol described in previous studies.[41] The QPPO solution was prepared by mixing QPPO, methanol, and dimethylformanide, of which the content is specified in ref 41. The as-prepared solution was used to infiltrate ACC, following a similar approach as the infiltration of Nafion, but the annealing temperature was changed to 90 °C. The mass of Nafion-infiltrated ACC increased to 0.95 g from 0.56 g, while that of QPPO-infiltrated ACC increased to 0.92 g. The infiltrated electrodes were then tailored to squares with a dimension of 6 × 6 cm^2, at the center of which a 1.6 × 1.6 cm^2 square hole was cut out. In the control experiment where ACC was used as received without further treatment other than washing with Milli-Q water, it was tailored to the identical shape as the infiltrated counterparts.

Material Characterization. The presence of the infiltration was confirmed by scanning electron microscopy (SEM) and elemental mapping. Both were obtained using an environmental FEI Quanta FEG 650 high-resolution scanning electron microscope that was equipped with an energy dispersive X-ray spectrometer. In addition, the pristine and infiltrated ACC electrodes were characterized using a Bruker Tensor 27 Fourier transform infrared spectrometer, with a total scanning rate of 256 scans/sample ranging from 400 to 4000 cm^{-1} at a resolution of 2 cm^{-1}. The specific surface areas of three types of ACC electrodes were determined by nitrogen adsorption at −196 °C using an Autosorb-iQ/MP. The surface area was calculated using the Brunauer−Emmett−Teller (BET) method.

Experimental Setup and Methods. MCDI stack consisted of two cells in parallel, each of which had two ACC electrodes, a glass fiber spacer, and an IEM at each side of the spacer (Figure 1). IEMs placed in front of the cathode and anode were Neosepta CMX (δ_{CMX} = 170 μm) and AMX (δ_{AMX} = 140 μm), respectively. Graphite foil (δ_{foil} = 130 μm) was used as the current collector (Alfa Aesar, USA). Similarly, two pairs of infiltrated ACC electrodes with spacers and current collectors made up the πCDI stack. Additional experiments involve a CDI stack that is essentially the same as the MCDI stack but without IEMs. The stacks were firmly compressed into the corresponding acrylic housing. The feed solution enters from the periphery of the stack and exits through the center hole. Right after the exit, an in-line conductivity meter (Edaq Isopod, Australia) was placed to continuously monitor the effluent conductivity, which was connected to a desktop for data acquisition. In the Supporting Information, a photographic illustration of the experimental apparatus is included (Figure S1). The raw data were converted to salt concentration based on a calibration curve. The feed solution was a 20 mM NaCl solution stored in a 10 L container which was continuously purged with nitrogen to remove dissolved oxygen. The feed solution was pumped through the cell housing, and the effluent was sent back to the feed reservoir. A potentiostat (SP 150, BioLogic, France) was employed to apply constant current in the charging step and zero voltage in the discharge step.

To evaluate the performance of πCDI in comparison with MCDI, the kinetic and energetic trade-off curves were constructed for both cells achieving the same diluted volume with the same concentration. The details of the experimental protocol have been described in previous studies.[34,42,43] The charging and discharging cycles were repeated at least three times to ensure dynamic steady states. The targeted average diluted concentration was 16.5 mM, and the diluted volume was 18 mL. A similar comparison between πCDI and CDI was also conducted.

Data Analysis. To check if the target adsorption is achieved, the average diluted concentration, $\overline{c}_D$, is calculated via the following equation

$$\overline{c}_D = \frac{\int_0^{t_c} c_D(t)\mathrm{d}t}{t_c} \tag{25}$$

where $c_D(t)$ is the effluent concentration in the charging step that changes with respect to time and t_c is the charging step duration.

Two performance metrics, specific energy consumption (SEC) and average salt adsorption rate (ASAR), are evaluated for both cells. SEC is defined as the energy consumed to remove a unit mole of NaCl

$$\mathrm{SEC} = \frac{\int_0^{t_c} IV(t)\mathrm{d}t}{Q\int_0^{t_c}(c_0 - c_D(t))\mathrm{d}t} \tag{26}$$

https://dx.doi.org/10.1021/acs.est.9b07692
Environ. Sci. Technol. 2020, 54, 5874−5883

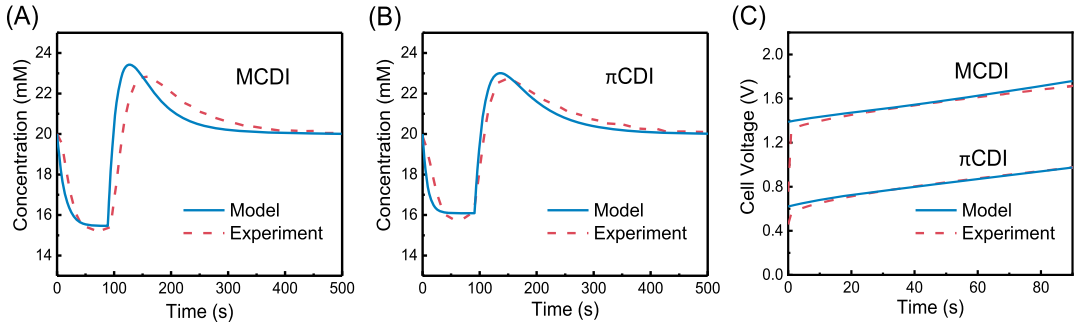

Figure 4. Effluent concentration as a function of time: MCDI (A) and πCDI (B). The corresponding cell voltage profiles in the charging step (C). The flowrate to the cell is 12 mL min^{-1} and the corresponding hydraulic residence time (HRT) is 17 s for both systems. The current densities are 1.50 and 1.76 mA cm^{-2}, respectively, for MCDI and πCDI. The volume and the concentration of the diluted streams are 18 mL and 16.5 mM, respectively, and the corresponding ASARs are around 22 μmol g^{-1} min^{-1}. The dashed curves are experimental data, while the solid curves are model results.

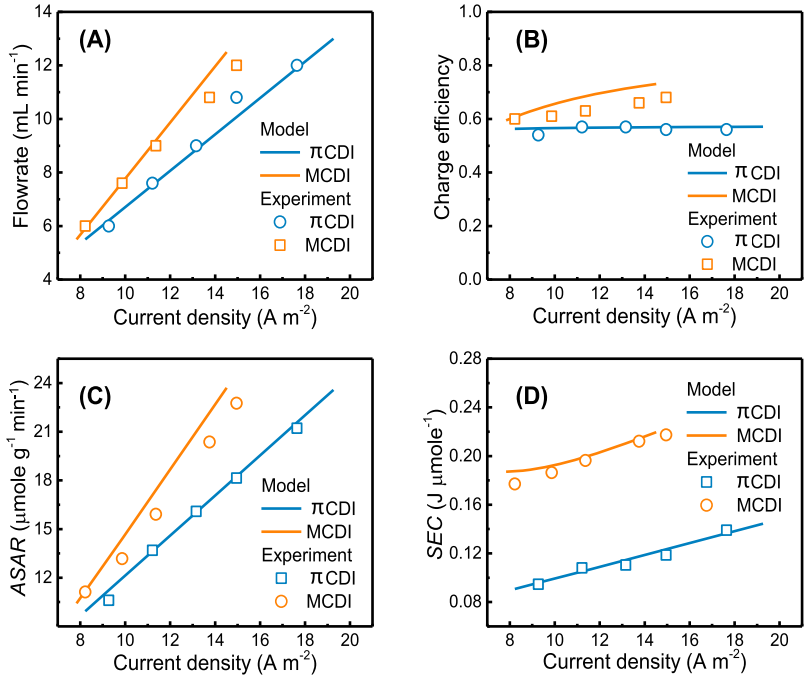

Figure 5. (A) Flowrate, (B) charge efficiency, (C) ASAR, and (D) SEC at different current densities for both MCDI (orange) and πCDI (blue). Feed solution of 20 mM is desalinated to 16.5 mM for all cases. Open squares and circles are experimental results of MCDI and πCDI, respectively, while the solid curves are obtained from modeling.

where I is the applied current during the charging stage, $V(t)$ is the corresponding cell voltage that is measured with the potentiostat, Q is the flowrate to the cell stack, and c_0 is the initial feed concentration. Alternatively, SEC^{-1}, the mass of salt removed when consuming unit energy, is utilized to construct the trade-off curves.

The deionization kinetics, average salt adsorption rate (ASAR), defined as the amount of salt removed during the charging step normalized by the product of electrode mass (W) and charging time.

$$\mathrm{ASAR} = \frac{Q\int_0^{t_c}(c_0 - c_D(t))\mathrm{d}t}{Wt_c} \tag{27}$$

RESULTS AND DISCUSSION

Experimental Results and Model Validation. The infiltration of the polyelectrolytes was successfully conducted. The freshly prepared ones were also analyzed with SEM, of which the results are summarized in the Supporting Information (Figures S2 and S3). More importantly, we characterized the πCDI electrodes after all the desalination experiments with SEM and energy dispersive X-ray spectrometry (EDS) elemental mapping to show the durability of the as-prepared electrodes (Figure 3). The pristine ACC electrode was mostly covered with carbon (Figure 3A,D) and with impurities coming from the surface oxidation, which is evidenced by the oxygen elemental mapping (Figure S4). The Nafion-infiltrated ACC fibers were covered with sulfur as the polyelectrolyte contains sulfonated groups (Figure 3B,E), and the wide-spread nitrogen on the QPPO-infiltrated electrode indicates the presence of the polyelectrolyte (it contains amine groups). In other words, the polyelectrolytes were still present in the electrodes after the desalination experiments. The dry weight of πCDI electrodes after the desalination experiments was 3.403 g, as a comparison, that

https://dx.doi.org/10.1021/acs.est.9b07692
Environ. Sci. Technol. 2020, 54, 5874−5883

before the experiments was 3.747 g. The total duration of the desalination experiments was about 5 h.

The successful infiltration of the polyelectrolyte was also confirmed by FTIR spectra (Figure S5). The presence of Nafion was verified by the characteristic peaks at ∼1150 and ∼1210 cm^{-1}, which correspond to the symmetric and asymmetric stretching of the CF_2 group, as well as the symmetric sulfonate (SO_3) stretching at 1060 cm^{-1}.[44] Similarly, comparing the FTIR spectra of QPPO-infiltrated and pristine ACC electrodes reveals the infiltration of QPPO from the characteristic peaks at 725 cm^{-1} (C−Cl stretching), 938 cm^{-1} (C−N), 1201 cm^{-1} (C−O−C stretching), 1400 cm^{-1} (CH_2 stretching), and 1600 cm^{-1} (C═C stretching).[45] After infiltration, the BET surface area decreases from 1548 m^2 g^{-1} (pristine) to 505.9 and 650.4 m^2 g^{-1} for Nafion- and QPPO-infiltrated electrodes, respectively (Figure S6). The discrepancy between the infiltrated electrodes in the surface area can be explained by the less stability of QPPO during the annealing step.[46]

In order to evaluate the performance of the πCDI in comparison with conventional MCDI, a series of experiments achieving the same target desalination were conducted for both cells. The target separation is specified by a c_0 of 20 mM, a $\bar{c}_D$ of 16.5 mM, and a diluted volume (V_D) of 18 mL. A typical cycle of πCDI and MCDI with constant current charging and zero voltage discharge is presented in Figure 4. Upon charging the cell with constant current, the effluent concentration reaches a plateau after the initial decrease. At the same time, the cell voltage keeps increasing until the charging step is terminated. To achieve the same V_D with the identical $\bar{c}_D$, a higher current density is needed for πCDI in comparison with MCDI, *that is*, 1.76 *versus* 1.50 mA cm^{-2}. However, the cell voltage in the πCDI is smaller than that in the MCDI, indicating smaller overall resistances in the πCDI system. In general, the model predicts the cell voltages and concentrations for both MCDI and πCDI very well. The parameter settings of the theoretical model are summarized in the Supporting Information (Table S1).

Performance Analysis. To systematically evaluate the performance of πCDI in comparison with MCDI, several sets of experiments operating with various flowrates (*i.e.,* HRT) and current densities achieving the same diluted concentration and volume were conducted for both MCDI and πCDI cells. Figure 5 presents the operating conditions and the experimental results from these experiments. To achieve the same $\bar{c}_D$, the flowrate increases nearly linearly with current density in both cells. In addition, the flowrate for MCDI is generally higher than that for πCDI when charging at the same current density (Figure 5A). In other words, a larger current density has to be applied for πCDI relative to MCDI when the flowrate to the spacer is the same. These phenomena indicate that a higher charge efficiency is attained in MCDI (Figure 5B), and the superiority becomes more notable at large current densities. The charge efficiency for πCDI is barely dependent on the current density or flowrate, while that for MCDI increases with the current density or flowrate (Figure 5C). The increasing charge efficiency in MCDI is mainly due to the increasing flowrate that diminishes the initial phase reaching the plateau concentration from the feed (Figure S7).[47] The charge efficiency achieved with MCDI is well within the range that is commonly observed in literature studies, which is mainly limited by the redox reactions and the surface charges on the ACC electrode surface.[35,48,49] When charging with the same current density, smaller kinetics, quantified by ASAR, is found in πCDI, with an enlarging difference at high current densities. Nevertheless, the SEC in πCDI is only about half of that in MCDI (Figure 5D) because of the infiltration of the highly charged polyelectrolyte. In general, the model successfully predicts the data very well for all the experiments, which demonstrates the credibility and reliability of the model for further analysis.

In previous studies, we employed energetic and kinetic trade-off curves to evaluate the performance of CDI with different operation modes, electrode materials, and configurations.[42] The same evaluation approach is adopted here to compare πCDI with MCDI. Briefly, trade-off curves were constructed for both processes achieving the same separation. Along each curve, it represents ASAR and the corresponding SEC^{-1} for that specific separation, and ASAR increases with decreasing SEC^{-1} and vice versa. When comparing different processes and each of them has a trade-off curve, any curve that sits above demonstrates a better energetic and kinetic performance than the other if these curves do not intersect. In the case that intersection occurs, we have to specify that one is better in one range, whereas the other is better in other ranges.

When comparing the curves of πCDI with MCDI (Figure 6), SEC^{-1} of πCDI is higher than that of MCDI in the range

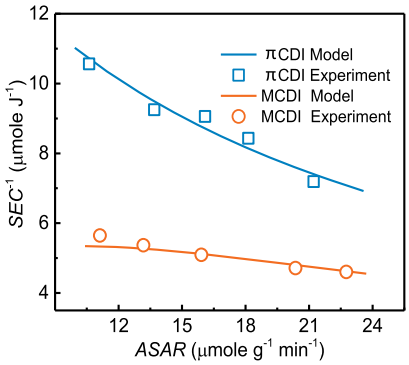

Figure 6. Energetic and kinetic trade-off curve of MCDI and πCDI for the charging stage. SEC^{-1} is the inverse of the SEC, and ASAR is the average salt adsorption rate. Solid curves are model results, while the open symbols are derived from experimental data. For all cases, a 20 mM feed solution is diluted to 16.5 mM and the diluted volume is 18 mL.

spanning from 10 to 24 μmol g^{-1} min^{-1}. The difference between the SEC^{-1}s for the two cells is more prominent in the lower end of ASAR. For instance, when achieving an ASAR of 10 μmol g^{-1} min^{-1}, SEC^{-1} of πCDI is 11 μmol J^{-1}, which doubles that of MCDI. Across the ASAR range, πCDI demonstrates a higher dependence of SEC^{-1} on ASAR in contrast to MCDI. Additional comparison between πCDI and CDI was carried out, of which the trade-off curves are summarized in the Supporting Information (S3 and Figure S8).

Comparison of Energy Breakdowns. Because there are multiple layers in the cells, the role of each in contributing to the energy reductions is not clear. In this section, we quantify the energy loss in each component and compare such breakdowns of the two systems, with the purpose of illustrating the improvement of πCDI in energy efficiency. We present the comparison of the breakdowns simulated from the theoretical models at two ASARs that are close to the lower and higher

https://dx.doi.org/10.1021/acs.est.9b07692
Environ. Sci. Technol. 2020, 54, 5874−5883

bounds of the range studied (Figure 7). Because the energy consumption is a function of the charging time, here, we only look at the SEC at the end of the charging step.

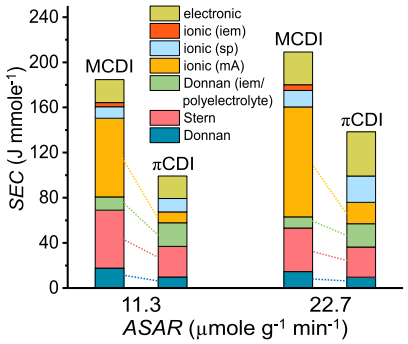

Figure 7. Comparison of the breakdown of SEC for MCDI and πCDI based on the models developed in this work. A separation from 20 to 16.5 mM is achieved for two ASARs, 11.3 and 22.7 μmol g^{-1} min^{-1}, respectively.

A close observation of the breakdowns reveals that the largest decrease from MCDI to πCDI occurs in the electrode macropores, which is attributed to the reduced impedance as the highly charged polyelectrolyte fills the macropores and attracts a large number of counterions. It reduces nearly seven times from 69.8 to 9.7 J mol^{-1} from MCDI to πCDI, respectively (orange area labeled "ionic (mA)" in Figure 7), which accounts for 70% of the total saved energy in πCDI from MCDI when operating at an ASAR of 11.3 μmol g^{-1} min^{-1}. Moreover, this reduction becomes more significant when achieving a higher ASAR. Other than the improvement in the macropores, the absence of IEMs in πCDI eliminates the potential drops and thus the energy consumption in the IEMs.

The resistance in the spacer is identical as both processes achieve the same diluted concentration in the spacer, assuming that there are no concentration profiles forming in the spacer channel and the hydrodynamic conditions have no effects. The potential drop in the spacer channel is then only dependent on the charge density. Because the slightly lower charge efficiency is with πCDI, a higher current density has to be applied and therefore higher energy consumption is found in the spacer, and this becomes more noticeable when achieving a higher ASAR that intrinsically requires a larger current density.

Another component that consumes more energy in πCDI than in MCDI is the Donnan potential at the two edges of the IEMs or the polyelectrolyte. In the πCDI, of which the macropores are filled with the highly charged polyelectrolyte, the counterion concentration in the macropores is quite high, rendering high Donnan potentials at the two ends of the polyelectrolyte-filled macropores. In contrast to the spacer, the energy consumption due to the Donnan potentials seem to be seldom dependent on the ASAR. When ASAR doubles from 11.3 to 22.7 μmol g^{-1} min^{-1}, the Donnan potential SEC stays around 20 and 10 J mol^{-1} for πCDI and MCDI, respectively.

Both microporous Donnan and Stern potentials build up as the ions are stored in the micropores and charges transferred to the electrode matrix. The Stern potential is directly related to the Stern capacitance and the micropore charge density.[50] Following the assumption that the charged polyelectrolyte does not penetrate into the electrode micropores, the property, *for example*, Stern capacitance, is considered identical in the model. Therefore, the different Stern layer potential drops and the energy consumptions result from the different micropore charge densities. By comparing the energy consumption by the Stern potential, πCDI spends less energy, indicating that the micropore charge densities in the πCDI is smaller, although it adsorbs the same amount of salt ions as the MCDI. With respect to the microporous Donnan potential, it is determined by the ion concentration ratios between the micropore and the macropore. The macropores of πCDI are filled with the charged polyelectrolyte which renders a high concentration of counterions in the macropores, and therefore, the Donnan potential and its energy consumption are smaller in πCDI in comparison with MCDI.

With respect to the equivalent circuit resistance (ESR) that includes the contact resistance between the electrode and the current collector and the external resistances in the electrical circuit, it is same for both processes, and its contribution to the total SEC is only proportional to the current density. As discussed before, the current density for πCDI is higher than that for MCDI to a small extent and the ESR SEC is about the same for both cells.

Implications. In this work, we report a method to improve the energy efficiency of the basic CDI setup by infiltrating the ion-conductive polyelectrolyte into the macropores of the electrode. The desalination experiment shows that the πCDI consumes much less energy than MCDI, while achieving the same target adsorption (same diluted concentration with the same volume). The theoretical model is developed for πCDI, where the polyelectrolyte-filled macropores are modeled as the charged ion-selective layer. The model is fitted to the experimental data and further employed to analyze the energy breakdowns for both πCDI and MCDI. It reveals that the energy consumption in the macropores is significantly reduced in πCDI along with the elimination of energy loss due to IEMs.

This study demonstrates that the macropores in the porous carbon electrodes undermine the energy efficiency of CDI. Technically speaking, the macropores barely contribute to the ion storage and are not necessary for ion removal in CDI. The weakness of the macropores could be circumvented essentially in two ways. One is to increase the ion concentration in the macropores. The other being eliminating the presence of macropores while keeping the pathways for ion transport. Therefore, a promising direction of electrode fabrication could be developing the electrode with majorly micropores and accessibility to ion movement. Our method is a combination of both approaches. The macropores are filled with the highly charged polyelectrolyte, which serves as bridges between the micropore and the feed channel (*i.e.,* spacer). The model developed in this study can be easily extended to future studies with similar endeavors. Although we use ACC as the platform for infiltration, this approach is expected to improve the performance of the activated carbon particle electrodes but needs to be further tested.

■ ASSOCIATED CONTENT

Supporting Information

The Supporting Information is available free of charge at https://pubs.acs.org/doi/10.1021/acs.est.9b07692.

Experimental cell setup; SEM images of freshly Nafion-infiltrated ACC; SEM images of freshly QPPO-infiltrated ACC; EDS impurity mapping of the pristine ACC electrode; FTIR spectra of pristine and infiltrated electrodes; nitrogen adsorption and desorption iso-

https://dx.doi.org/10.1021/acs.est.9b07692
Environ. Sci. Technol. 2020, 54, 5874−5883

therms as a function of relative pressure; effluent concentrations of MCDI as a function of time; trade-off curves of πCDI and CDI; and parameter settings for the theoretical model (PDF)

AUTHOR INFORMATION

Corresponding Authors

Li Wang − *Department of Civil and Environmental Engineering, Vanderbilt University, Nashville, Tennessee 37235-1831, United States;* orcid.org/0000-0002-5542-6696; Email: li.wang.1@vanderbilt.edu

Li Zhang − *Wetsus, European Centre of Excellence for Sustainable Water Technology, 8911 MA Leeuwarden, The Netherlands;* orcid.org/0000-0003-2836-794X; Email: li.zhang@wetsus.nl

Author

Yuanzhe Liang − *Department of Civil and Environmental Engineering, Vanderbilt University, Nashville, Tennessee 37235-1831, United States*

Complete contact information is available at: https://pubs.acs.org/10.1021/acs.est.9b07692

Notes

The authors declare no competing financial interest.

ACKNOWLEDGMENTS

L.W. acknowledges the support from the National Science Foundation via research grant 1739884. This work is performed in the cooperation framework of Wetsus, European Centre of Excellence for Sustainable Water Technology. Wetsus is cofunded by the Dutch Ministry of Economic Affairs and the Ministry of Infrastructure and Environment, the Province of Fryslân, and the Northern Netherlands Provinces. The authors would like to thank Dr. Shihong Lin and Dr. P. M. Biesheuvel for their invaluable discussion and suggestions. The authors also thank Mingqian Li from UCSD for helping in the specific surface area measurement.

REFERENCES

(1) Porada, S.; Zhao, R.; van der Wal, A.; Presser, V.; Biesheuvel, P. M. Review on the science and technology of water desalination by capacitive deionization. *Prog. Mater. Sci.* **2013**, *58*, 1388−1442.

(2) Długołęcki, P.; van der Wal, A. Energy Recovery in Membrane Capacitive Deionization. *Environ. Sci. Technol.* **2013**, *47*, 4904−4910.

(3) Rommerskirchen, A.; Linnartz, C. J.; Müller, D.; Willenberg, L. K.; Wessling, M. Energy Recovery and Process Design in Continuous Flow Electrode Capacitive Deionization Processes. *ACS Sustainable Chem. Eng.* **2018**, *6*, 13007−13015.

(4) Kang, J.; Kim, T.; Shin, H.; Lee, J.; Ha, J.-I.; Yoon, J. Direct energy recovery system for membrane capacitive deionization. *Desalination* **2016**, *398*, 144−150.

(5) Ji, F.; Wang, L.; Yang, J. S.; Wu, X.; Li, M. Q.; Jiang, S. L.; Lin, S. H.; Chen, Z. Highly compact, free- standing porous electrodes from polymer- derived nanoporous carbons for efficient electrochemical capacitive deionization. *J. Mater. Chem. A* **2019**, *7*, 1768−1778.

(6) Yin, H.; Zhao, S.; Wan, J.; Tang, H.; Chang, L.; He, L.; Zhao, H.; Gao, Y.; Tang, Z. Three-Dimensional Graphene/Metal Oxide Nanoparticle Hybrids for High-Performance Capacitive Deionization of Saline Water. *Adv. Mater.* **2013**, *25*, 6270−6276.

(7) Wang, H.; Zhang, D.; Yan, T.; Wen, X.; Zhang, J.; Shi, L.; Zhong, Q. Three-dimensional macroporous graphene architectures as high performance electrodes for capacitive deionization. *J. Mater. Chem. A* **2013**, *1*, 11778−11789.

(8) Wang, H.; Shi, L.; Yan, T.; Zhang, J.; Zhong, Q.; Zhang, D. Design of graphene-coated hollow mesoporous carbon spheres as high performance electrodes for capacitive deionization. *J. Mater. Chem. A* **2014**, *2*, 4739−4750.

(9) Gao, X.; Omosebi, A.; Landon, J.; Liu, K. Enhanced Salt Removal in an Inverted Capacitive Deionization Cell Using Amine Modified Microporous Carbon Cathodes. *Environ. Sci. Technol.* **2015**, *49*, 10920−10926.

(10) Gao, X.; Omosebi, A.; Landon, J.; Liu, K. Surface charge enhanced carbon electrodes for stable and efficient capacitive deionization using inverted adsorption-desorption behavior. *Energy Environ. Sci.* **2015**, *8*, 897−909.

(11) Gao, X.; Omosebi, A.; Holubowitch, N.; Liu, A.; Ruh, K.; Landon, J.; Liu, K. Polymer-coated composite anodes for efficient and stable capacitive deionization. *Desalination* **2016**, *399*, 16−20.

(12) Arulrajan, A. C.; Ramasamy, D. L.; Sillanpaa, M.; van der Wal, A.; Biesheuvel, P. M.; Porada, S.; Dykstra, J. E. Exceptional Water Desalination Performance with Anion-Selective Electrodes. *Adv. Mater.* **2019**, *31*, 1806937.

(13) Kim, S.; Yoon, H.; Shin, D.; Lee, J.; Yoon, J. Electrochemical selective ion separation in capacitive deionization with sodium manganese oxide. *J. Colloid Interface Sci.* **2017**, *506*, 644−648.

(14) Yang, J.; Zou, L.; Choudhury, N. R. Ion-selective carbon nanotube electrodes in capacitive deionisation. *Electrochim. Acta* **2013**, *91*, 11−19.

(15) Liu, Y.; Ma, W.; Cheng, Z.; Xu, J.; Wang, R.; Gang, X. Preparing CNTs/Ca-Selective zeolite composite electrode to remove calcium ions by capacitive deionization. *Desalination* **2013**, *326*, 109−114.

(16) Hawks, S. A.; Cerón, M. R.; Oyarzun, D. I.; Pham, T. A.; Zhan, C.; Loeb, C. K.; Mew, D.; Deinhart, A.; Wood, B. C.; Santiago, J. G.; Stadermann, M.; Campbell, P. G. Using Ultramicroporous Carbon for the Selective Removal of Nitrate with Capacitive Deionization. *Environ. Sci. Technol.* **2019**, *53*, 10863−10870.

(17) Mubita, T. M.; Dykstra, J. E.; Biesheuvel, P. M.; van der Wal, A.; Porada, S. Selective adsorption of nitrate over chloride in microporous carbons. *Water Res.* **2019**, *164*, 114885.

(18) Kim, S.; Lee, J.; Kim, C.; Yoon, J. Na2FeP2O7 as a Novel Material for Hybrid Capacitive Deionization. *Electrochim. Acta* **2016**, *203*, 265−271.

(19) Nam, D.-H.; Choi, K.-S. Bismuth as a New Chloride-Storage Electrode Enabling the Construction of a Practical High Capacity Desalination Battery. *J. Am. Chem. Soc.* **2017**, *139*, 11055−11063.

(20) Dykstra, J. E.; Zhao, R.; Biesheuvel, P. M.; van der Wal, A. Resistance identification and rational process design in Capacitive Deionization. *Water Res.* **2016**, *88*, 358−370.

(21) Wang, L.; Dykstra, J. E.; Lin, S. Energy Efficiency of Capacitive Deionization. *Environ. Sci. Technol.* **2019**, *53*, 3366−3378.

(22) Dykstra, J. E.; Porada, S.; van der Wal, A.; Biesheuvel, P. M. Energy consumption in capacitive deionization - Constant current versus constant voltage operation. *Water Res.* **2018**, *143*, 367−375.

(23) Hemmatifar, A.; Palko, J. W.; Stadermann, M.; Santiago, J. G. Energy breakdown in capacitive deionization. *Water Res.* **2016**, *104*, 303−311.

(24) Kim, Y.-J.; Choi, J.-H. Enhanced desalination efficiency in capacitive deionization with an ion-selective membrane. *Sep. Purif. Technol.* **2010**, *71*, 70−75.

(25) Zhao, R.; Biesheuvel, P. M.; van der Wal, A. Energy consumption and constant current operation in membrane capacitive deionization. *Energy Environ. Sci.* **2012**, *5*, 9520−9527.

(26) Lee, J.-B.; Park, K.-K.; Eum, H.-M.; Lee, C.-W. Desalination of a thermal power plant wastewater by membrane capacitive deionization. *Desalination* **2006**, *196*, 125−134.

(27) Tandon, R.; Pintauro, P. N. Divalent/monovalent cation uptake selectivity in a Nafion cation-exchange membrane: Experimental and modeling studies. *J. Membr. Sci.* **1997**, *136*, 207−219.

(28) Pintauro, P. N.; Tandon, R.; Chao, L.; Xu, W.; Evilia, R. Equilibrium Partitioning of Monovalent Divalent Cation-Salt

Mixtures in Nafion Cation-Exchange Membranes. *J. Phys. Chem.* **1995**, *99*, 12915−12924.
(29) Ryoo, M.-W.; Seo, G. Improvement in capacitive deionization function of activated carbon cloth by titania modification. *Water Res.* **2003**, *37*, 1527−1534.
(30) Bhat, A. P.; Reale, E. R.; del Cerro, M.; Smith, K. C.; Cusick, R. D. Reducing impedance to ionic flux in capacitive deionization with Bi-tortuous activated carbon electrodes coated with asymmetrically charged polyelectrolytes. *Water Res. X* **2019**, *3*, 100027.
(31) Fritz, P. A.; Boom, R. M.; Schroen, K. Polyelectrolyte-activated carbon composite electrodes for inverted membrane capacitive deionization (iMCDI). *Sep. Purif. Technol.* **2019**, *220*, 145−151.
(32) Biesheuvel, P. M.; Hamelers, H. V. M.; Suss, M. E. Theory of Water Desalination by Porous Electrodes with Immobile Chemical Charge. *Colloid Interface Sci. Commun.* **2015**, *9*, 1−5.
(33) Gao, X.; Porada, S.; Omosebi, A.; Liu, K.-L.; Biesheuvel, P. M.; Landon, J. Complementary surface charge for enhanced capacitive deionization. *Water Res.* **2016**, *92*, 275−282.
(34) Wang, L.; Lin, S. Theoretical framework for designing a desalination plant based on membrane capacitive deionization. *Water Res.* **2019**, *158*, 359−369.
(35) Mubita, T. M.; Porada, S.; Biesheuvel, P. M.; van der Wal, A.; Dykstra, J. E. Capacitive deionization with wire-shaped electrodes. *Electrochim. Acta* **2018**, *270*, 165−173.
(36) Zhang, L.; Biesheuvel, P. M.; Ryzhkov, I. I. Theory of Ion and Water Transport in Electron-Conducting Membrane Pores with pH-Dependent Chemical Charge. *Phys. Rev. Appl.* **2019**, *12*, 014039.
(37) Biesheuvel, P. M. Two-fluid model for the simultaneous flow of colloids and fluids in porous media. *J. Colloid Interface Sci.* **2011**, *355*, 389−395.
(38) Tedesco, M.; Hamelers, H. V. M.; Biesheuvel, P. M. Nernst-Planck transport theory for (reverse) electrodialysis: I. Effect of co-ion transport through the membranes. *J. Membr. Sci.* **2016**, *510*, 370−381.
(39) Lopez-Ramon, M. V.; Stoeckli, F.; Moreno-Castilla, C.; Carrasco-Marin, F. On the characterization of acidic and basic surface sites on carbons by various techniques. *Carbon* **1999**, *37*, 1215−1221.
(40) Boehm, H. P. Some Aspects of the Surface-Chemistry of Carbon-Blacks and Other Carbons. *Carbon* **1994**, *32*, 759−769.
(41) Huang, C.-C.; Yang, M.-S.; Liang, M. Synthesis of new thermosetting poly(2,6-dimethyl-1, 4-phenylene oxide)s containing epoxide pendant groups. *J. Polym. Sci., Part A: Polym. Chem.* **2006**, *44*, 5875−5886.
(42) Wang, L.; Lin, S. Intrinsic tradeoff between kinetic and energetic efficiencies in membrane capacitive deionization. *Water Res.* **2018**, *129*, 394−401.
(43) Wang, L.; Lin, S. Membrane Capacitive Deionization with Constant Current vs Constant Voltage Charging: Which Is Better? *Environ. Sci. Technol.* **2018**, *52*, 4051−4060.
(44) Dai, Z.; Ansaloni, L.; Ryan, J. J.; Spontak, R. J.; Deng, L. Nafion/IL hybrid membranes with tuned nanostructure for enhanced CO2 separation: effects of ionic liquid and water vapor. *Green Chem.* **2018**, *20*, 1391−1404.
(45) Kim, J.-H.; Ryu, S.; Lee, J.-Y.; Moon, S.-H. Preparation of high-conductivity QPPO (quaternary-aminated poly (2,6-dimethyl-1,4-phenyleneoxide)) membranes by electrical treatment. *J. Membr. Sci.* **2018**, *553*, 82−89.
(46) Hou, J.; Wang, X.; Liu, Y.; Ge, Q.; Yang, Z.; Wu, L.; Xu, T. Wittig reaction constructed an alkaline stable anion exchange membrane. *J. Membr. Sci.* **2016**, *518*, 282−288.
(47) Hawks, S. A.; Knipe, J. M.; Campbell, P. G.; Loeb, C. K.; Hubert, M. A.; Santiago, J. G.; Stadermann, M. Quantifying the flow efficiency in constant-current capacitive deionization. *Water Res.* **2018**, *129*, 327−336.
(48) Duan, F.; Du, X.; Li, Y.; Cao, H.; Zhang, Y. Desalination stability of capacitive deionization using ordered mesoporous carbon: Effect of oxygen-containing surface groups and pore properties. *Desalination* **2015**, *376*, 17−24.
(49) Zhang, C.; He, D.; Ma, J.; Tang, W.; Waite, T. D. Faradaic reactions in capacitive deionization (CDI) - problems and possibilities: A review. *Water Res.* **2018**, *128*, 314−330.
(50) Wang, L.; Biesheuvel, P. M.; Lin, S. Reversible Thermodynamic Cycle Analysis for Capacitive Deionization with Modified Donnan Model. *J. Colloid Interface Sci.* **2018**, *512*, 522.

NOTE ADDED AFTER ASAP PUBLICATION

This paper was published ASAP on April 17, 2020, with an incorrect word in the title. The corrected version was reposted on April 20, 2020.

https://dx.doi.org/10.1021/acs.est.9b07692
Environ. Sci. Technol. 2020, 54, 5874−5883